Monthly Notices of the ROYAL ASTRONOMICAL SOCIETY

MNRAS **537,** 1182–1196 (2025) https://doi.org/10.1093/mnras/staf066
Advance Access publication 2025 January 14

# Quantifying the impact of the Si/O interface in CCSN explosions using the Force Explosion Condition

Luca Boccioli [1]★ Mariam Gogilashvili [2] Jeremiah Murphy [3] and Evan P. O'Connor [4]

[1]*Department of Physics, University of California, Berkeley, CA 94720, USA*
[2]*Niels Bohr International Academy and DARK, Niels Bohr Institute, University of Copenhagen, Blegdamsvej 17, DK- 2100 Copenhagen, Denmark*
[3]*Department of Physics, Florida State University, 77 Chieftan Way, Tallahassee, FL 32306, USA*
[4]*Department of Astronomy, The Oskar Klein Centre, Stockholm University, AlbaNova, SE-106 91 Stockholm, Sweden*

Accepted 2025 January 10. Received 2025 January 10; in original form 2024 October 22

## ABSTRACT

The explosion mechanism of a core-collapse supernova (SN) is a complex interplay between neutrino heating and cooling (including the effects of neutrino-driven convection), the gravitational potential, and the ram pressure of the infalling material. To analyse the post-bounce phase of an SN, one can use the generalized force explosion condition (FEC+), which succinctly formalizes the interplay among these four phenomena in an analytical condition, consistent with realistic simulations. In this paper, we use the FEC+ to study the post-bounce phase of 341 spherically symmetric simulations, where convection is included through a time-dependent mixing-length approach. We find that the accretion of the Si/O interface through the expanding shock can significantly change the outcome of the SN by driving the FEC+ above the explosion threshold. We systematically explore this by (i) artificially smoothing the pre-SN density profile, and (ii) artificially varying the mixing length. In both cases, we find that large-enough density contrasts at the Si/O interface lead to successful shock revival only if the FEC+ is already close to the explosion threshold. Furthermore, we find that the accretion of the Si/O interface has a substantial effect on the critical condition for SN explosions, contributing between 5 and 15 per cent, depending on how pronounced the density contrast at the interface is. Earlier studies showed that convection affects the critical condition by 25–30 per cent, which demonstrates that the accretion of the Si/O interface through the shock can play a nearly comparable role in influencing shock dynamics.

**Key words:** convection – hydrodynamics – neutrinos – shock waves – stars: evolution – transients: supernovae.

## 1 INTRODUCTION

The explosion mechanism of a core-collapse supernova (CCSN) has been the topic of many decades of research (Colgate & White 1966; Bethe & Wilson 1985; Burrows & Goshy 1993; Herant et al. 1994; Fryer & Warren 2002; Janka 2012; Müller 2016; Burrows & Vartanyan 2021). Theoretical, observational, and computational efforts have shed light on to this complex phenomenon, and the theoretical understanding of the explosion of a CCSN has drastically improved in the last decade, thanks to the rapid improvement of supercomputers and, therefore, of detailed simulations (Fernández 2015; Lentz et al. 2015; Takiwaki, Kotake & Suwa 2016; Cabezón et al. 2018; Summa et al. 2018; O'Connor & Couch 2018b; Glas et al. 2019; Burrows et al. 2020; Bollig et al. 2021; Nakamura et al. 2024).

None the less, the detailed mechanism of the CCSN explosion is still a matter of active research. Understanding the physical phenomena that lead to an explosion has important consequences in a variety of astrophysical environments. Knowing which stars explode and which ones fail determines the distribution of compact objects in the Universe (Fryer et al. 2012; Patton & Sukhbold 2020; Fryer, Olejak & Belczynski 2022; Boccioli & Fragione 2024). It also determines the thermodynamic conditions that lead to the nucleosynthesis of heavy elements, which, in turn, determines the chemical enrichment of the interstellar medium (Woosley, Heger & Weaver 2002; Diehl et al. 2021). Finally, understanding the physical phenomena responsible for triggering the explosion can unveil what are the pre-collapse features that are important for the explosion or the failed shock revival (Boccioli et al. 2023).

The first breakthrough in studying the CCSN explosion mechanism was made by Colgate & White (1966), who suggested that neutrinos were responsible for carrying energy from the deep interior of the central protoneutron star (PNS) to the vicinity of the shock. Later, Bethe & Wilson (1985) refined this picture by introducing the so-called delayed neutrino mechanism. In their simulations, neutrinos take a few hundred milliseconds after the bounce to transfer enough energy to revive the shock. During this period, the shock stalls at a nearly constant radius. However, with more advanced models for describing the state of matter at supranuclear densities and interactions between neutrinos and matter (Bruenn 1985; Lattimer & Swesty 1991), the explosion could not be obtained in spherical symmetry anymore. The reason is the lack of multidimensional effects, and state-of-the-art multidimensional simulations indeed show self-consistent explosions (Couch et al. 2015; Lentz et al. 2015; Summa et al. 2018; Burrows et al. 2020; Bollig et al. 2021; Nakamura et al. 2024). In particular, in the last two decades, neutrino-driven

★ E-mail: lbocciol@berkeley.edu

convection has been shown to play a crucial role for the explosion dynamics (Foglizzo, Scheck & Janka 2006; Murphy, Dolence & Burrows 2013; Abdikamalov et al. 2015; Radice et al. 2016, 2018). The importance of this effect motivated the development of parametric models to include neutrino-driven convection and turbulent dissipation effects in spherically symmetric, 1D simulations. These parametric models are known as 1D+ simulations and over the years, they were able to produce successful explosions (Mabanta & Murphy 2018; Couch, Warren & O'Connor 2020; Boccioli, Mathews & O'Connor 2021; Sasaki & Takiwaki 2024).

The advantage of such models is that they are computationally very affordable, and therefore allow for systematic studies of the explosion mechanism itself. One of the first attempts at deriving an explosion condition was the seminal work of Burrows & Goshy (1993), who derived a critical luminosity condition based on the idea that, given a mass accretion rate, there is a maximum neutrino luminosity above which a stalled shock solution is not realizable, and therefore an explosion can develop. Similar studies were later carried out over the years (Yamasaki & Yamada 2005; Murphy & Burrows 2008; Janka 2012; Pejcha & Thompson 2012; Summa et al. 2016, 2018; Murphy & Dolence 2017; Gogilashvili & Murphy 2022), oftentimes guided by the results of multidimensional simulations.

Recently, a few studies (Wang et al. 2022; Boccioli et al. 2023) have pointed out that the magnitude of the density drop located near the Si/O interface can be used to predict the outcome of the explosion. Even before these studies, the idea that the accretion of the Si/O interface on to the shock could facilitate the explosion was well established (references). Because of the sudden change in composition, there is usually a large density drop at the Si/O interface that, when accreted through the shock, leads to a sudden drop in ram pressure, facilitating a rapid shock expansion that, under the right conditions, can turn into a runaway explosion.

In this paper, we will analyse how the accretion on to the shock of the density drop, which typically occurs near the Si/O interface, affects the explosion. In particular, this manuscript is structured as follows: in Section 2.1, we describe the FEC+, in Section 2.2 we discuss the accretion of the Si/O interface through the shock, and in Section 2.3 we describe our numerical setup. Then, in Section 3, we analyse the explosion of 341 1D+ simulations, and in Section 4 we study how the strength of neutrino-driven convection and the magnitude of the density drop at the Si/O interface change the FEC+ and therefore the explosion. Finally, we discuss the results in Section 6.

## 2 METHODS

### 2.1 The generalized force explosion condition

Over the years many have suggested explosion criteria for successful CCSN explosions (Pejcha & Thompson 2012; Ertl et al. 2016; Müller et al. 2016a; Wang et al. 2022; Boccioli et al. 2023). Over three decades ago, Burrows & Goshy (1993) pointed out that the stalled shock phase is a steady-state, boundary-value problem. They parameterized this problem by the neutrino luminosity, $L_\nu$, and mass accretion rate, $\dot{M}$, and they found a critical curve in these parameters, below which stalled shock solutions exist and above this critical curve there are no steady-state solutions. They suggested that the solutions above this critical curve are most likely explosive.

Inspired by the insight of Burrows & Goshy (1993), Murphy & Dolence (2017) utilized semi-analytic techniques to propose an integral condition for SN explosions. This work suggests that the dimensional integral of the momentum equation, denoted as $\Psi$, is helpful for determining the existence of stalled-shock solutions. The relationship between the shock velocity and the parameter $\Psi$ indicates that a stalled solution exists if $\Psi = 0$. This force explosion condition is consistent with critical neutrino luminosity conditions and 1D simulations and implies that more factors than just neutrino luminosity and mass accretion rate influence explosion dynamics. They show that the integral explosion condition corresponds to a critical hypersurface where the physical dimensions are $L_\nu$, $M_{\rm NS}$, $R_{\rm NS}$, and $\dot{M}$.

Gogilashvili & Murphy (2022) derived an analytic model for the force explosion condition, beginning with fundamental hydrodynamic equations and identifying that the explosion condition depends on two dimensionless parameters instead of four-dimensional parameters. The force explosion condition (FEC) is expressed as

$$\tilde{L}_\nu \tau_g - a\tilde{\kappa} \geq b, \tag{1}$$

where $\tilde{L}_\nu \tau_g = L_\nu \tau_g R_{\rm NS}/(G\dot{M}M_{\rm NS})$ represents the net neutrino power normalized by accretion power, and $\tilde{\kappa} = \kappa \dot{M}/\sqrt{GM_{\rm NS}R_{\rm NS}}$ is a dimensionless neutrino opacity. The coefficients $a$ and $b$ mostly depend upon the density profile of the material behind the shock and can be estimated analytically to be $a \sim 0.05$ and $b \sim 0.51$. It is crucial to emphasize that the theory provides an analytic functional form of the FEC. While the coefficients can be estimated analytically, these estimates might not be accurate due to the approximations and assumptions of the model and thus might need proper calibration with CCSN simulations.

Note that in this work we use the net neutrino heating rate in the gain region per unit time $\tilde{Q}_\nu$ in place of the first term in equation (1) $\tilde{L}_\nu \tau_g$, as done in Gogilashvili, Murphy & O'Connor (2023b) when using self-consistent simulations to calculate the FEC. The reason behind this is that in the original semi-analytical FEC formulation, the term $L_\nu \tau_g$ is meant to represent the net neutrino heating rate in the gain region $\dot{Q}_\nu$, which can, however, be directly calculated from our simulations.

The validity of the FEC has been checked through three approaches. Gogilashvili & Murphy (2022) first, compared the FEC with the semi-analytic condition of Burrows & Goshy (1993), leading to a numerical fit for $a = 0.06$ and $b = 0.38$, which closely matched their analytical estimates. Second, they demonstrated that the FEC accurately predicts explosion conditions in 1D light-bulb simulations. In follow-up research, Gogilashvili et al. (2023b) adapted the FEC for simulations using actual neutrino transport, such as those conducted with the `GR1D` code (O'Connor & Ott 2010; O'Connor 2015). Their tests confirmed that the FEC reliably predicts explosion conditions in spherically symmetric SN simulations, highlighting its robustness as a diagnostic tool.

Motivated by the accuracy of the spherical force explosion condition, Gogilashvili, Murphy & Miller (2023a) generalized the FEC to incorporate multidimensional effects such as neutrino-driven convection and turbulent dissipation in a simple model. This generalized condition, termed FEC+, is expressed as

$$\tilde{Q}_\nu + \tilde{W}_b - a\tilde{\kappa} + c\left\langle \tilde{R}^r_r \right\rangle = b. \tag{2}$$

It depends on two additional dimensionless parameters: $\tilde{W}_b = W_b R_{\rm NS}/(G\dot{M}M_{\rm NS})$, representing the dimensionless buoyant driving, and $\tilde{R}^r_r = R^r_r R_{\rm NS}/(GM_{\rm NS})$, representing the dimensionless Reynolds stress. These additional terms (mostly buoyant driving) reduce the net neutrino heating required for explosion by 26 per cent, a reduction consistent with published studies (Murphy & Meakin 2011; Murphy et al. 2013; Mabanta & Murphy 2018). This finding highlights the significance of multidimensional effects in SN explosion dynamics.

Consequently, the FEC+ offers a more comprehensive and accurate framework for describing the explodability of multidimensional simulations, enhancing our understanding of the underlying physical processes.

As mentioned above, in the simple spherically symmetric case the coefficients in equation (1) can be fitted using a simple steady-state model, as derived by Gogilashvili & Murphy (2022). However, for the more complicated model that includes convection (i.e. the FEC+ in equation 2), a more accurate calibration is needed, and the same holds for applying the FEC+ to multidimensional simulations. For this paper, we therefore explicitly calculate the coefficients $a$ and $c$ in equation (2) based on the expressions found in appendix A of Gogilashvili et al. (2023a). As a consequence, there is as yet no *a priori* derivation of the threshold value, i.e. the coefficient $b$. Instead, we empirically determine the threshold $b$ by analysing hundreds of 1D+ simulations in the next section. In practice, the threshold is found to be around 0.28–0.3.

### 2.2 The role of the Si/O interface accretion

The presence of density discontinuities in the pre-SN progenitor can play a significant role in the explosion (Ertl et al. 2016; Tsang, Vartanyan & Burrows 2022; Wang et al. 2022; Boccioli et al. 2023). In particular, the density discontinuity located near the Si/O interface is responsible for triggering the explosion in the vast majority of progenitors. However, as we will quantitatively show in the remainder of this paper, the accretion of this interface on to the shock triggers the explosion only if the star is already close to exploding (in other words, the FEC+ is close to the threshold). This requires multidimensional effects and is therefore only possible in 2D, 3D, or 1D+ simulations. Specifically, Wang et al. (2022) and Boccioli et al. (2023) found that one can build a criterion based on the density drop at the Si/O interface that can successfully predict the explodability of $>90$ per cent progenitors. In particular, both studies independently showed that when the density drop is such that $\delta\rho^2_{\rm Si/O}/\rho^2_{\rm Si/O} > 0.08$ (Boccioli et al. 2023) [or, equivalently, $\delta P_{\rm ram}/P_{\rm ram} > 0.28$ (Wang et al. 2022)], an explosion will ensue. However, for high compactness progenitors, which are more common at low metallicities, Boccioli & Fragione (2024) showed that, even in the absence of this density drop, a successful shock revival would still occur, hinting that the explosion mechanism for these high-compactness stars is slightly different.

The Si/O interface usually occurs in correspondence with a pocket of oxygen inside the silicon-sulfur shell, which is why it should more precisely be referred to as a Si/O interface. For the sake of brevity, we will, however, refer to it simply as a Si/O interface in the remainder of this paper. Usually, the shock reaches this interface a few hundred milliseconds (typically 100–400 ms) after bounce, i.e. during the stalled shock phase. The sudden drop in density causes the ram pressure of the infalling material to suddenly decrease, and the shock is therefore able to expand to larger radii. Under favourable conditions, this expansion turns into a runaway explosion, causing a successful shock revival. This has been shown by several multidimensional simulations in the past few years (Lentz et al. 2015; Summa et al. 2016; Andresen et al. 2017; Burrows et al. 2020; Müller 2020; Nakamura, Takiwaki & Kotake 2022; Nakamura et al. 2024), where a successful shock revival occurs right after the shock reaches the Si/O interface. Note that, especially for 2D simulations, there are instances where the Si/O interface is accreted at times between 200 and 400 ms after bounce and the explosion instead is triggered much later, at times between 700 ms and 1 s (Marek & Janka 2009; O'Connor & Couch 2018a). Moreover, both in 2D and 3D simulations, different nuclear equations of state can lead to earlier or later explosions, depending on the details of the microphysics (Eggenberger Andersen et al. 2021; Janka & Bauswein 2023).

This suggests that, after the interface is accreted on to the shock, if the change in ram pressure is large enough to disrupt the quasi-steady state, then an explosion will occur. Otherwise, the perturbation might be large enough to move the standing accretion shock to larger radii, but not large enough to completely disrupt the quasi-steady state. In that case, the shock will stall at larger radii and, eventually, it will slowly recede and the explosion will fail (with a few exceptions, as discussed in Section 3.1). In the remainder of this paper, we will quantitatively test this hypothesis using the generalized force explosion condition (hereafter FEC+) described in Section 2.1.

### 2.3 Numerical setup

To analyse how the accretion of the Si/O interface affects the explosion, we employed a series of simulations performed with the open-source code `GR1D` (O'Connor & Ott 2010; O'Connor 2015), modified as described in Boccioli et al. (2021) to include the effect of neutrino-driven convection via the Reynolds decomposition model based on time-dependent mixing-length theory STIR (Couch et al. 2020). The equation of state for all simulations is the SFHo equation of state for nuclear matter (Hempel & Schaffner-Bielich 2010; Steiner, Hempel & Fischer 2013), and neutrino opacities from Bruenn (1985), with weak-magnetism and recoil corrections from Horowitz (2002), and the virial correction for neutrino-nucleon scattering from Horowitz et al. (2017). Neutrino-electron-scattering opacities follow the inelastic treatment of (Bruenn 1985). The neutrino transport solves the two-moment equations and uses the analytic M1 closure scheme to relate the radiation pressure to the radiation energy density and momentum (O'Connor 2015). The neutrino spectrum is resolved with 18 energy groups logarithmically spaced from 1 to 280 MeV.

The spatial resolution was the same for all of the simulated progenitors (with the only exception of $<10$ progenitors of very low compactness, with $M_{\rm ZAMS} < 11$). We adopted a grid of 700 zones linearly spaced up to 20 km, with a resolution of 300 m, and then logarithmically spaced out to 15 000 km. The decision to use the same spatial grid for all progenitors was motivated by the fact that the extra heating from STIR has a weak dependence on the spatial resolution, as shown in Boccioli et al. (2022), particularly behind the shock.

### 2.4 The STIR model

The STIR model (Couch et al. 2020) is based on a Reynolds decomposition of the Euler equations, and it relies on a mixing-length-like closure that relates higher order turbulent correlations to lower order turbulent correlations. The STIR model is a local algebraic model for which the equations are closed using algebraic relationships at a local level. Other models explored different closures (Murphy et al. 2013; Mabanta, Murphy & Dolence 2019; Müller 2019).

The main modification that STIR introduces is to the internal energy equation, although extra diffusive terms must also be added to the equations describing the evolution of the electron fraction and the neutrino energy. STIR evolves the internal energy and the turbulent energy separately, and therefore the evolution equation of the total energy is the combination of those two (i.e. equations 26

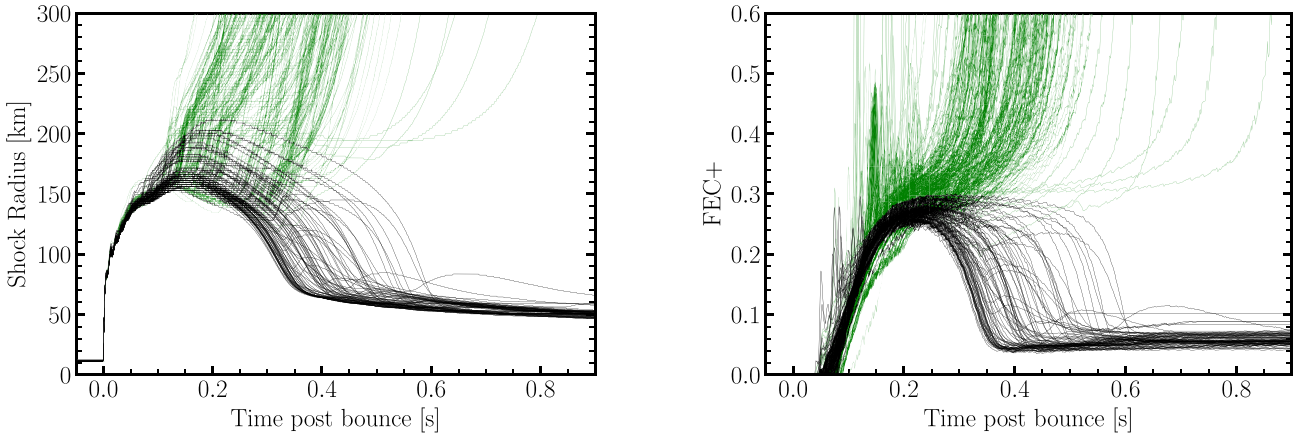


(a) (b)

**Figure 1.** This Figure shows the shock evolution (left panel) and FEC+ (right panel) of the collapse and subsequent post-bounce evolution computed by (Boccioli & Fragione 2024) of 341 progenitors at three different metallicities. Green lines indicate progenitors with successful shock revival, whereas black lines indicate progenitors for which the explosion has not been launched. There is a clear bifurcation in FEC+ , and empirically it can be seen that progenitors who reach a threshold around $\sim$ 0.28–0.3 explode. Those that do not reach this threshold do not explode.

and 29 from Couch et al. 2020):

$$\frac{\partial(\rho e_{\rm tot})}{\partial t} + \frac{1}{r^2}\frac{\partial}{\partial r}[r^2 v_r(\rho e_{\rm tot} + P + P_{\rm turb}) - r^2 \rho D \nabla e_{\rm tot}] = -\rho v_r g + Q_\nu - \rho v_{\rm turb}^2 \frac{\partial v_r}{\partial r} + \rho v_{\rm turb} \omega_{\rm BV}^2 \Lambda_{\rm mix}. \quad (3)$$

where $e_{\rm tot} = e + v_{\rm turb}^2$, and $P_{\rm turb} = \rho v_{\rm turb}^2$. In the above equations, $e$ includes the contributions from both internal and kinetic energy. Note that `GR1D` solves the general relativistic version of the above equation, but we show the Newtonian version for simplicity. The quantities $\omega_{\rm BV}$ and $\Lambda_{\rm mix}$ are the Brunt–Väisälä frequency and the mixing length, respectively, defined as

$$\omega_{\rm BV}^2 = \left(g - v\frac{\partial v}{\partial r}\right)\left(\frac{1}{\rho}\frac{\partial \rho(1+\epsilon)}{\partial r} - \frac{1}{\rho c_s^2}\frac{\partial P}{\partial r}\right), \quad (4)$$

$$\Lambda_{\rm mix} = \alpha_{\rm MLT}\frac{P}{\rho g}, \quad (5)$$

where we again have not included most of the general relativistic corrections, for simplicity. However, it should be highlighted that one should use the total energy $\rho(1+\epsilon)$ in the expression of the Brunt–Väisälä frequency, as shown in equation (4), rather than simply $\rho$. This can change the magnitude of the Brunt–Väisälä by more than 20 per cent. Equations (4) and (5) also show the dependence of STIR on the main parameter of the model: $\alpha_{\rm MLT}$. A larger value of $\alpha_{\rm MLT}$ increases the magnitude of the mixing length, which as can be seen from equation (3) corresponds to introducing a larger source of turbulent energy, and therefore stronger convection and subsequent explosion.

The extra terms due to STIR are the last two terms on the RHS of equation (3), and the last two terms on the LHS. The terms on the LHS, i.e. the diffusive terms, have a smaller (although non-negligible) effect on the overall dynamics compared to the terms on the RHS (Sasaki & Takiwaki 2024). If one applies the FEC+ to this model (Gogilashvili et al. 2023a), then one finds that $\tilde{W}_b$ in equation (2) corresponds to the last term on the RHS of equation (3), whereas $\langle \tilde{R}_r^r \rangle$ corresponds to the advection of $P_{\rm turb}$ in equation (3). Note that the shear term (i.e. the third term on the RHS of equation 3), is quite small, and therefore ignored in the expression of the FEC+.

## 3 EXPLOSION DYNAMICS OF 341 PROGENITORS

One of the primary aims of this manuscript is to use FEC+ to understand why the Si/O interface facilitates an explosion for most 1D+ STIR simulations and why the Si/O interface does not trigger explosions for other progenitors. The simulations for this study are described in Boccioli & Fragione (2024). In particular, Fig. 1 shows the evolution of the shock radius and the FEC+ for 341 `GR1D+` simulations of KEPLER progenitors from Sukhbold et al. (2016) and Woosley et al. (2002), with masses ranging from 9 to 120 $M_\odot$ and metallicities of $z = 0$, $z = 10^{-4} z_\odot$, and $z = z_\odot$, where $z_\odot$ indicates solar metallicity. The solid-green curves show simulations that eventually explode, and the black curves show simulations that fail to explode. The most striking feature in the FEC+ plot (right panel) is that there is a clear separation between failed and successful explosions for a value of FEC+ around 0.28–0.3. This is yet another example showing that the FEC+ can be used as an explosion diagnostic.

Although the definition of a successful explosion can vary, in this manuscript, we define a successful shock revival when the shock crosses 500 km. We will be using the same definition for the explosion time in Section 5. All of the simulations that show a successful shock revival also have positive diagnostic energies $E_{\rm diag}^+$, where

$$E_{\rm diag}^+ = \int_{e_{\rm bind}>0} e_{\rm bind} {\rm d}V - E_{\rm ov}, \quad (6)$$

where $e_{\rm bind}$ is the binding energy of the material and the integral is performed only over regions with positive binding energy (Buras et al. 2006; Bruenn et al. 2009). Note that we subtracted the binding energy (i.e. thermal energy minus gravitational energy) of the yet unshocked material ($E_{\rm ov}$) to have a more realistic estimate of the final explosion energy. The explosion energies at the end of the simulations of the 341 progenitors described above are shown in Fig. 2. Given the relatively small radial domain of the simulations, the shock leaves the boundary before the diagnostic energy has plateaued, especially in the case of high-compactness progenitors, and therefore Fig. 2 represents a lower limit to the final explosion energy.

In 1D simulations, the mass accretion is shut off once the shock is revived, and therefore neutrino heating drops to zero,

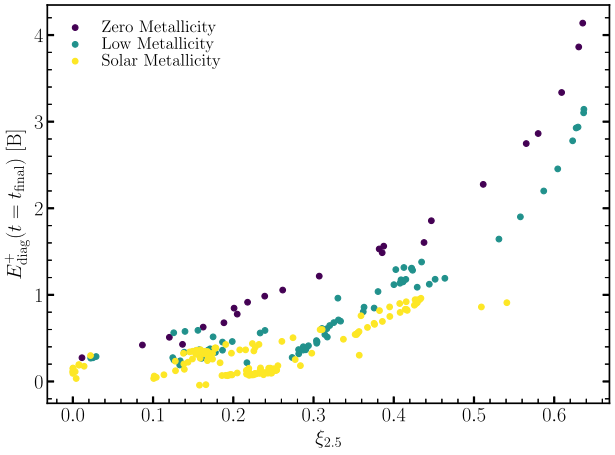


**Figure 2.** Explosion energy calculated at the end of the simulations, as defined by equation (6). This represents a lower limit of the explosion energy, since when the shock leaves the computational domain the diagnostic energy is still increasing. As expected the explosion energy increases with the progenitor compactness. The apparent trends of lower metallicity yielding large explosion energies for high-compactness progenitors, however, might be due to the aforementioned small computational domain preventing the diagnostic energy to plateau. Therefore, simulations with a larger radial domain (currently underway) are needed before drawing robust conclusions regarding the difference in explosion energy for progenitors of different metallicities.

even though a central black hole never forms. However, multidimensional simulations show that continued accretion after shock revival can be quite significant. This causes neutrino heating to be nonzero even after shock revival, potentially leading to larger explosion energies compared to 1D simulations (Burrows, Wang & Vartanyan 2024). However, in the case of high-compactness progenitors, continued accretion causes an early collapse to a black hole, completely shutting off neutrino emission that, in some cases (Powell, Müller & Heger 2021; Eggenberger Andersen et al. 2024; Sykes & Müller 2024), can lead to a decrease of the final explosion energy. Overall, one can still see in Fig. 2 that the explosion energy in 1D+ simulations increases with the compactness of the progenitor, as also seen in multidimensional simulations (Burrows et al. 2018).

It is also instructive to analyse the ratio of non-exploding models compared to observational constraints. To do that, we assumed that stars below $11\,{\rm M}_{\odot}$ (i.e. the lowest mass simulated for the $z = 0$ and $z = 10^{-4} z_{\odot}$ progenitors) would produce a successful explosion. Then, we weighted our simulations based on their initial zero-age main sequence mass using a Salpeter initial mass function with exponent $-2.35$ (Salpeter 1955), independently of metallicity. We calculated the fraction of failed SNe to be $f_{\rm fSNe} = 0.25 - 0.3$, depending on whether we assume the lowest mass of a star that explodes as a CCSN to be 8 or $9\,{\rm M}_{\odot}$, respectively (see fig. 6 in Boccioli & Fragione 2024). This is consistent with the observed fraction of failed SNe $f_{\rm fSNe} = 0.16^{+0.23}_{-0.12}$ (Neustadt et al. 2021).

In the remainder of this paper, we will use the FEC+ to diagnose why the Si/O interface can help facilitate explosions in many, but not all, successful explosions.

### 3.1 Pre-explosion phase in light of the FEC+

For the present analysis, we analyse the post-bounce phase of the aforementioned 341 simulations. The role of the Si/O interface can be divided into three categories: (1) the accretion of the Si/O interface through the shock immediately triggers a vigorous explosion, (2) the accretion of the interface triggers outward movement of the shock, the shock stalls again, retreats a little, and then explodes, (3) the accretion of the interface triggers outward progression of the shock, which subsequently stalls again and does not explode.

Generally, what determines which category a specific progenitor belongs to is how large the density drop at the Si/O interface is, and how late the interface is accreted. We consider a 'large' interface one characterized by $\delta\rho^2_{\rm Si/O}/\rho^2_{\rm Si/O} > 0.08$, consistent with the explodability criterion derived independently by Boccioli et al. (2023) and Wang et al. (2022), as summarized in Section 2.2. Moreover, in some high compactness ($\xi_{2.0}$) cases, explosions occur regardless of the accretion of the density drop. The compactness is defined as (O'Connor & Ott 2011)

$$\xi_{\rm M} = \frac{M/{\rm M}_{\odot}}{R(M)/1000\,{\rm km}}, \tag{7}$$

where $R(M)$ is the radial coordinate that encloses a mass $M$.

In (Boccioli et al. 2023)

Therefore, one can identify six different scenarios, shown by select simulations in Fig. 3, that describe the post-bounce evolution of both exploding and non-exploding models:

(i) A high-compactness progenitor, with $\xi_{2.0} \gtrsim 0.5$, achieves an explosion during the stalled phase independently of the presence of a large density drop in the pre-SN profile. This constitutes $\sim 26$ per cent of all the analysed simulations, including the 40 $\rm M_{\odot}$ progenitor shown in Fig. 3.

(ii) A progenitor with $\xi_{2.0} \lesssim 0.5$ achieves an explosion right after the accretion of a large density drop *during* the stalled-shock phase. This constitutes $\sim 45$ per cent of all the analysed simulations, including the $20\,{\rm M}_{\odot}$ progenitor shown in Fig. 3.

(iii) A progenitor with $\xi_{2.0} \lesssim 0.5$ achieves an explosion significantly after the accretion of a large density drop *before* the stalled-shock phase. This constitutes $\sim 2-3$ per cent of all the analysed simulations, including the $19.5\,{\rm M}_{\odot}$ progenitor shown in Fig. 3.

(iv) A progenitor with $\xi_{2.0} \lesssim 0.5$ fails to explode because it accretes a large (but not large enough) density drop *before* the stalled-shock phase. This constitutes $\sim 4-5$ per cent of all the analysed simulations, including the $15.5\,{\rm M}_{\odot}$ progenitor shown in Fig. 3. Note that these progenitors are very similar to the ones from the previous category but have smaller density drops (or the accretion occurs earlier).

(v) A progenitor with $\xi_{2.0} \lesssim 0.5$ fails to explode because it accretes a small density drop *during* the stalled-shock phase. This constitutes $\sim 4-5$ per cent of all the analysed simulations, including the $12.5\,{\rm M}_{\odot}$ progenitor shown in Fig. 3.

(vi) A progenitor with $\xi_{2.0} \lesssim 0.5$ fails to explode because it accretes either a small or large density drop *after* the stalled-shock phase. This constitutes $\sim 15$ per cent of all the analysed simulations, including the $18.2\,{\rm M}_{\odot}$ progenitor shown in Fig. 3.

The remaining $\sim 3-4$ per cent of the analysed simulations are outliers. For example, four progenitors with large compactness do not explode, whereas 10 progenitors with large Si/O interfaces accreted towards the beginning or the end of the stalled-shock phase do not explode. It is worth noting here that while these outliers do not conform to the Si/O interface condition for explosion, all simulations are consistent with the FEC+ explosion condition, i.e. the FEC+ never crosses the threshold. Perhaps the most interesting outlier is the $24.2\,{\rm M}_{\odot}$ progenitor with $z = 10^{-4} z_{\odot}$, which accretes a large density drop very late (and therefore is expected to fail) but instead leads

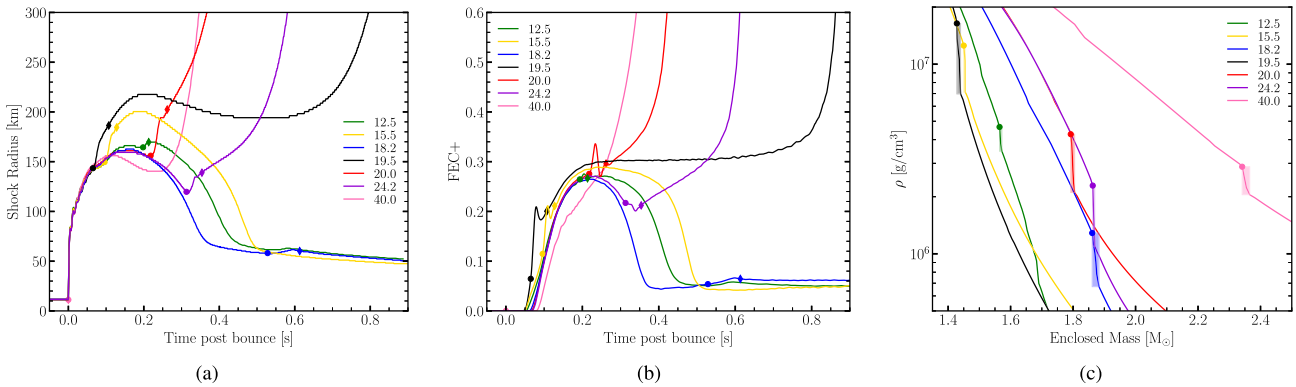


**Figure 3.** This figure shows the shock evolution, FEC+, and pre-collapse density structure of selected progenitors from the suite of 341 analysed in this paper. Each progenitor is an example of a different explosive and non-explosive scenario, as discussed in the text (see Section 3.1). Moreover, we also show the 24.2 $M_\odot$ which does not fall in any of those scenarios, and it also has a very peculiar time-evolution of the FEC+, which quickly dips similarly to what happens in failed SNe, before suddenly increasing after the accretion of the Si/O interface, which, however, does not seem to affect the FEC+ . In the left and middle panels, circles and diamonds mark the times before and after the accretion of the Si/O interface, respectively. See Section 4.1 for a description of how these times are defined. The right panel shows the pre-SN density profiles for all of the progenitors, zoomed in near the Si/O interface. Circles mark the inner edge of the Si/O interface (which is used to define the time when the accretion stars $t_{\rm accr}^{\rm start}$), and the shaded regions show the extent of the interface. Note that progenitors with lower compactness, have steeper density profiles.

to a successful explosion. We include this progenitor in Fig. 3 to highlight the unusual time-evolution of the FEC+ and shock radius. Two more progenitors, i.e. the 23.4 and 23.2 $M_\odot$ with $z = 10^{-4} z_\odot$ have a similar pre-SN structure and post-bounce evolution. However, these progenitors have high compactness ($\xi_{2.0} > 0.5$), and the Si/O interface is accreted a bit earlier. Therefore their shock radius and FEC+ time-evolution are not quite as unusual as they are for the 24.2 $M_\odot$ progenitor. In other words, the FEC+ is not far from the threshold when the explosion sets in, whereas it clearly is for the 24.2 $M_\odot$ progenitor.

Since the FEC+ represents a clear threshold for explosion, and we know exactly which components contribute to its evolution, it is also a useful diagnostic to understand why the accretion of the Si/O interface initiates explosion when it does. In the two leftmost panels of Fig. 3, we indicated the time before and after the accretion of the Si/O interface (hereafter $t_{\rm accr}^{\rm start}$ and $t_{\rm accr}^{\rm end}$, respectively) with circles and diamonds. We define $t_{\rm accr}^{\rm start}$ as the time when the inner side of the Si/O interface is accreted through the shock. A more detailed description of how we define $t_{\rm accr}^{\rm end}$ is given later in Section 4.1. In the following, we analyse the FEC+ evolution for each of the above scenarios, showcased in Fig. 3.

The 40 $M_\odot$ progenitor accretes the Si/O interface significantly after the explosion has started. Therefore, the accretion of the Si/O interface does not play a role whatsoever in the explosion of this progenitor. This is confirmed by the smooth evolution of the FEC+ , without any rapid increase caused by the accretion of the Si/O interface. What distinguishes this progenitor is its large pre-SN compactness $\xi_{2.0} = 0.75$ that causes the neutrino heating to be very large, which drives the FEC+ to go above the threshold and trigger the explosion. A more thorough analysis of the role of compactness in triggering the explosion is currently underway and beyond the scope of this paper.

The 20 $M_\odot$ progenitor has a large density drop at the Si/O interface, and therefore the shock revival is more pronounced than, for example, in the case of the 12.5 $M_\odot$ progenitor. This translates into a large increase of the FEC+ that is pushed above the threshold, indicating that an explosion occurs.

The 12.5 $M_\odot$ has a small density drop which is reflected in a small increase in the FEC+. However, this increase is not large enough to push the FEC+ above the threshold, and therefore the explosion eventually fails.

The 18.2 $M_\odot$ has a large density drop, which is, however, accreted at $\sim$ 500 ms post-bounce, after the stalled-shock phase of the shock has ended. As can be seen from the left panel of Fig. 3 the shock radius quickly recedes at very small radii after $\sim$ 250–300 ms. Therefore, even though a large interface is accreted at late times, the shock cannot be revived anymore. In multidimensional simulations, where not only neutrino-driven convection but also other instabilities and asymmetries can develop, the stalled-shock phase might be longer and/or more asymmetric, which could change the outcome of the simulation.

The 19.5 $M_\odot$ progenitor shows a unique behaviour. A very large density drop is accreted early in the evolution. However, since the FEC+ is still small when the accretion occurs, it does not increase enough to go above the threshold. Therefore, the explosion is not triggered after the accretion of the interface, and in principle, one would expect the explosion to fail. However, since this early accretion causes the shock to stall at larger radii than any of the other progenitors, the FEC+ at around 150−200 ms is the largest among the progenitors shown. Therefore, between 200 and 300 ms, the FEC+ is barely below the threshold. Eventually, at around 600–700 ms, the FEC+ finally goes above the threshold causing a (relatively) late explosion.

One can speculate about what the cause of the explosion is. For most progenitors, it is the accretion of the Si/O interface that directly launches the explosion by reducing the ram pressure on the shock. For this specific progenitor (as well as a handful of others), the explosion happens much later than the accretion. None the less, the early accretion of the Si/O interface still plays a crucial role in causing the explosion. This can be seen by comparing the shock radius and FEC+ evolution for the 19.5 $M_\odot$ and the 15.5 $M_\odot$ progenitors. These have almost identical pre-SN density (and also compositional) structures, as seen in the third panel of Fig. 3, with the important difference that the 15.5 $M_\odot$ progenitor has a smaller density drop at the Si/O interface, and also a Si shell that is 0.125 $M_\odot$ thicker, causing the interface to be accreted at a slightly later time. The smaller density drop causes the shock radius and the FEC+ to have a smaller increase, and therefore the FEC+ during the stalled-shock phase (i.e.

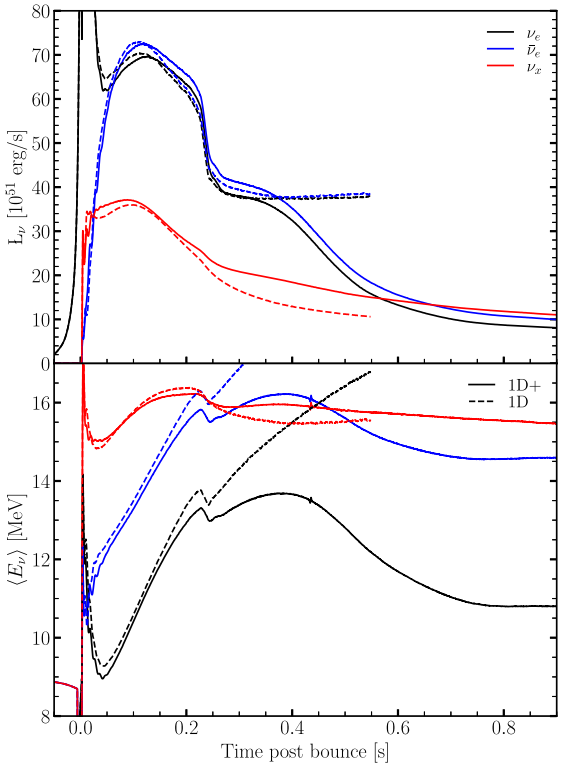


**Figure 4.** The top panel shows the total net neutrino heating in the gain region for the set of progenitors discussed in Section 3.1. The bottom panel shows the ratio of the advection and heating time-scales. Solid and dashed lines indicate simulations with and without STIR, respectively. Circles mark the times when the Si/O interface is accreted through the shock for the simulations with STIR. To avoid clutter, and since it occurs essentially at the same time, we did not mark the time of accretion of the Si/O interface for the simulations without STIR. The ratio of time-scales, as expected, has some similarities to the FEC+ shown in the middle panel of Fig. 3. However, as discussed in the text the FEC+ is a more robust, less ambiguous condition.

at $\sim$ 200 ms after bounce) is smaller for the 15.5 $M_\odot$ progenitor. This is the reason why the 15.5 $M_\odot$ progenitor fails whereas the 19.5 $M_\odot$ progenitor explodes at a much later time.

Another interesting feature of these two progenitors is that, since they have a very similar post-bounce evolution, the shock trajectory of the 15.5 $M_\odot$ progenitor would look pretty much exactly like the one for the 19.5 $M_\odot$ progenitor if one were to use a larger value of $\alpha_{\rm MLT}$. This shows that most CCSNe are in general very close to explosion, and small changes in the physics can lead to qualitatively drastically different outcomes.

In order to better illustrate the explosion dynamics of 1D+ models, we show in Fig. 4 the average energies and luminosities for both a 1D and a 1D+ simulation of a 20 $M_\odot$ progenitor from Sukhbold et al. (2016), i.e. the same shown in Fig. 3. The neutrino quantities for electron neutrinos and antineutrinos are quite similar in the 1D and 1D+ simulations since they are mostly determined by post-bounce mass accretion history, which is the same in 1D and 1D+ until the explosion sets in at around $\sim$ 220 ms in the 1D+ model, causing mass accretion to stop and therefore neutrino energies and luminosities to decrease. In the case of heavy-lepton neutrinos, however, both average energies and luminosities are instead larger in the 1D+ model after the explosion sets in. This can be explained by the fact that heavy-lepton neutrinos are produced deeper in the PNS, and therefore are much less dependent on the accretion history of the progenitor (O'Connor 2015).

The increase in the luminosity of heavy-lepton neutrinos at late times in 1D+ models can be attributed to PNS convection, which pushes the neutrinosphere at larger radii, increasing the area of emission, and therefore the luminosity. The reason for the larger neutrino energies in 1D+ simulations is instead more subtle. Convection in the PNS smooths out the density gradient, and therefore deep in the PNS, between $\sim 10^{13}$ and $10^{14}$ g cm$^{-3}$, the density gradient in the 1D case is shallower, whereas near the neutrinosphere, between $\sim 10^{12}$ and $10^{13}$ g cm$^{-3}$, it is steeper. The shallower gradient deep inside the PNS in the 1D simulation causes larger energy losses due to inelastic scattering, explaining the lower neutrino energies. This effect is subdominant for electron-flavor neutrinos since beta processes dominate the opacity.

A heuristic condition often used to determine whether an explosion sets in is based on the ratio of heating and advection time-scales (Janka 2001; Thompson, Quataert & Burrows 2005; Buras et al. 2006; Murphy & Burrows 2008; Marek & Janka 2009; Fernández 2012). A few different definitions of these two quantities are possible, and we adopt the following:

$$\tau_{\rm adv} = \frac{M_{\rm gain}}{\dot{M}}, \qquad \tau_{\rm heat} = \frac{E_{\rm gain}}{\dot{Q}_\nu}, \tag{8}$$

where $E_{\rm gain}$, $M_{\rm gain}$, and $\dot{M}$ are the thermal energy, total mass, and average mass accretion rate in the gain region, respectively. It has been proposed that successful shock revival occurs when $\tau_{\rm adv}/\tau_{\rm heat} > 1$ (Thompson et al. 2005). Note that some groups Summa et al. (2018) define $E_{\rm gain}$ as the total energy in the gain region (i.e. thermal plus kinetic plus gravitational) instead of the thermal energy only. However, in our case using the total energy results in the ratio $\tau_{\rm adv}/\tau_{\rm heat}$ to increase above 1 slightly earlier (and in some cases much earlier) than when shock revival occurs. This ambiguity is part of the reason why a more fundamental condition like the FEC+ should be preferred. We show the ratio of these two time-scales in Fig. 5, where one can also see the difference in adopting STIR (solid lines) compared to a simple 1D simulation (dashed lines). Essentially, convection allows the shock to stall at a larger radius, causing neutrino heating to increase (i.e. $\tau_{\rm heat}$ to decrease) driving $\tau_{\rm adv}/\tau_{\rm heat}$ above 1. A more detailed study on how convection enables neutrino heating to increase is currently underway and is beyond the scope of this paper.

In the next section, we will investigate how changes in the strength of $\nu$-driven convection (i.e. changes in $\alpha_{\rm MLT}$) and in the density drop at the Si/O interface can change the shock and the evolution of the FEC+, leading to a successful or failed explosion. It is important to remark that also changes in the nuclear equation of state, neutrino opacities, asymmetries in the pre-SN progenitor, beyond standard model physics, collective neutrino oscillations, and more, in general, any physical input of the simulation, can lead to similar differences in the outcome of the SN.

Since numerical simulations are involved, not only changes to the physics but also changes to the numerical setup and algorithms can lead to different outcomes. For example, as mentioned in the previous section, STIR has a weak dependence on resolution. Therefore, not only changes to $\alpha_{\rm MLT}$, but also changes to the numerical resolution can lead to an explosion for the higher resolution simulation and a failed SN for the lower resolution simulation. This can be generalized to the case of multidimensional simulations, where numerical resolution is well known to create different rates of turbulent dissipation (Couch & Ott 2015; Radice et al. 2016, 2018), which can therefore affect the explodability.

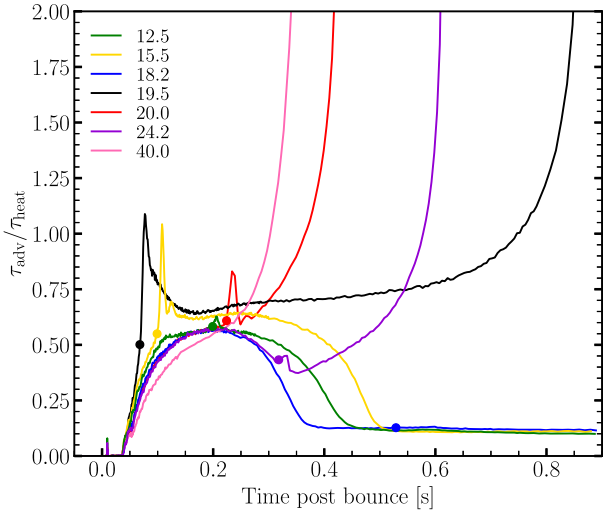


**Figure 5.** The top panel shows the total net neutrino heating in the gain region for the set of progenitors discussed in Section 3.1. The bottom panel shows the ratio of the advection and heating time-scales. Solid and dashed lines indicate simulations with and without STIR, respectively. Circles mark the times when the Si/O interface is accreted through the shock for the simulations with STIR. To avoid clutter, and since it occurs essentially at the same time, we did not mark the time of accretion of the Si/O interface for the simulations without STIR. The ratio of time-scales, as expected, has some similarities to the FEC+ shown in the middle panel of Fig. 3. However, as discussed in the text the FEC+ is a more robust, less ambiguous condition.

To summarize, we qualitatively observed three types of explosions: (i) the ones triggered directly by the accretion of the Si/O interface (like the 20 $M_\odot$ in Fig. 3), which causes a significant shock expansion and drives the FEC+ above the threshold, hence causing the explosion; (ii) the ones triggered indirectly by the accretion of the Si/O interface (like the 19.5 $M_\odot$ in Fig. 3), where the accretion of this layer causes a significant shock expansion and pushes the FEC+ very close to the threshold until it eventually goes above and triggers the explosion; (iii) the ones triggered by a rapid increase of the FEC+, which occurs in high-compactness progenitors such as the 40 $M_\odot$ in Fig. 3, not caused by accretions of any significant density drops, but simply a very strong neutrino heating.

Most importantly, in all cases analysed the explosion occurs after the FEC+ goes above $\sim$ 0.28–0.3, despite the qualitative difference in how the FEC+ crosses this threshold, which shows the robustness and flexibility of the FEC+ as a diagnostic tool to determine the onset of explosion (but see the 24.2 $M_\odot$ progenitor as an exception to this statement).

## 4 INTERPLAY BETWEEN NEUTRINO-DRIVEN CONVECTION AND ACCRETION OF THE SI/O INTERFACE

As shown in the previous section, the accretion of the Si/O interface can often lead to the explosion of a CCSN. In this section, we use the FEC+ to quantify in detail how the post-accretion expansion of the shock depends on both the strength of $\nu$-driven convection and the density drop at the Si/O interface. In addition to being an explosion condition, the FEC+ can also quantify a distance from explosion. Therefore, it is useful as a quantitative measure of how various physics affect the explosion outcome. It should be highlighted that, in a more realistic 3D simulation, other multidimensional effects are also at play, and therefore the post-bounce phase is more complicated.

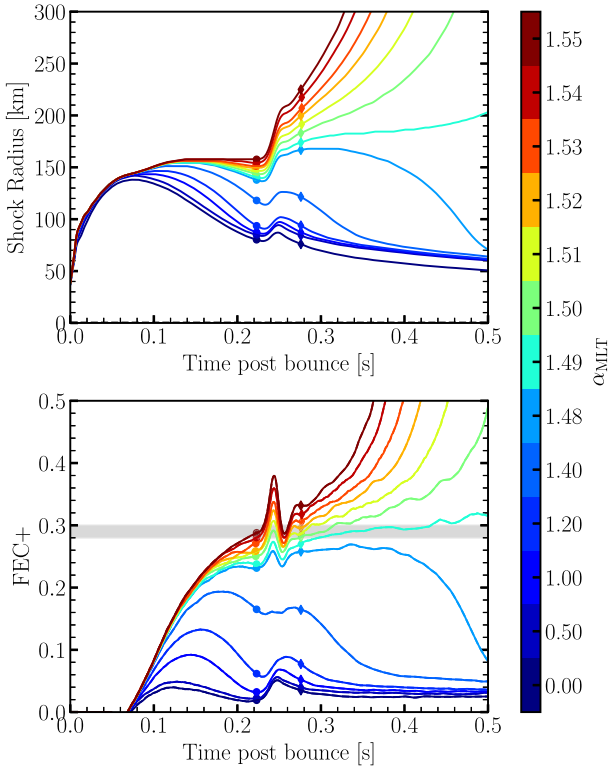


**Figure 6.** The top (bottom) panel shows the evolution of the shock radius (FEC+) for a 20 $M_\odot$ MESA progenitor (Farmer et al. 2016) whose collapse was simulated using GR1D+ for different values of $\alpha_{\rm MLT}$, shown in the colour bar on the right. Before calculating the value of the FEC+ , each quantity in equation (2) has been smoothed with a Savitzky–Golay filter in a 10 ms window. The filled dots show the time before the accretion of the Si/O interface, whereas the filled diamonds show the time after the accretion of the Si/O interface. All of the simulations with $\alpha_{\rm MLT} \geq 1.495$ successfully explode, and the accretion of the Si/O interface leads to a larger increase of the FEC+ for larger values of $\alpha_{\rm MLT}$. To avoid cluttering, we only show exploding simulations with $\alpha_{\rm MLT}$ spaced by 0.01, but a finer grid is shown in Figs 7 and 8.

However, the simplicity of 1D+ simulations enables a systematic study of the interplay between the accretion of the Si/O interface and parametrized $\nu$-driven convection.

### 4.1 Sensitivity to the strength of neutrino-driven convection

To analyse the interplay between (parameterized) neutrino-driven convection and the accretion of the Si/O interface, one can analyse how the FEC+ changes as a function of $\alpha_{\rm MLT}$. Therefore, we simulated the collapse and subsequent explosion of a 20 $M_\odot$ from Farmer et al. (2016) for different values of $\alpha_{\rm MLT}$. This progenitor is particularly interesting as it is characterized by a large density drop at the Si/O interface. The shock evolution and the FEC+ as a function of time after bounce are shown in Fig. 6. As in Fig. 1, one can see that there is a threshold for the FEC+ around 0.28–0.3 that separates explosions from failed SNe. As expected, simulations with small values of $\alpha_{\rm MLT}$ are further away from the threshold, and fail to explode. Simulations with large values of $\alpha_{\rm MLT}$ cross the critical threshold and lead to a successful explosion.

For the accretion of the Si/O interface to be sufficient to launch the explosion, the FEC+ has to be already close to the threshold. This is shown in the top panel of Fig. 7, where the $x$-axis is the value of the

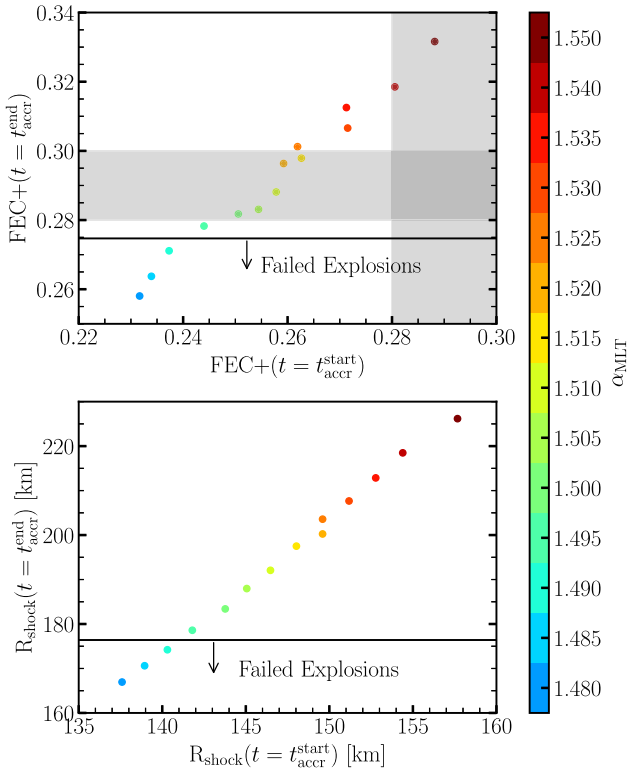


**Figure 7.** The top panel shows the values of the FEC+ at $t = t^{start}_{accr}$ ($x$-axis) and at $t = t^{end}_{accr}$ ($y$-axis) the accretion of the Si/O interface through the shock. The times before and after accretion are shown as circles and diamonds in Fig. 6. For a description of how exactly the times before and after accretion are defined, see the text. Only simulations with $\alpha_{MLT} \geq 1.48$ are shown, since in other cases the FEC+ and shock radius do not show any significant 'jumps'. Simulations below the horizontal bar yield failed explosions, and indeed only when the FEC+ at $t = t^{end}_{accr}$ has crossed the threshold an explosion ensues. The bottom panel is the same as the top one but for shock radius instead of FEC+.

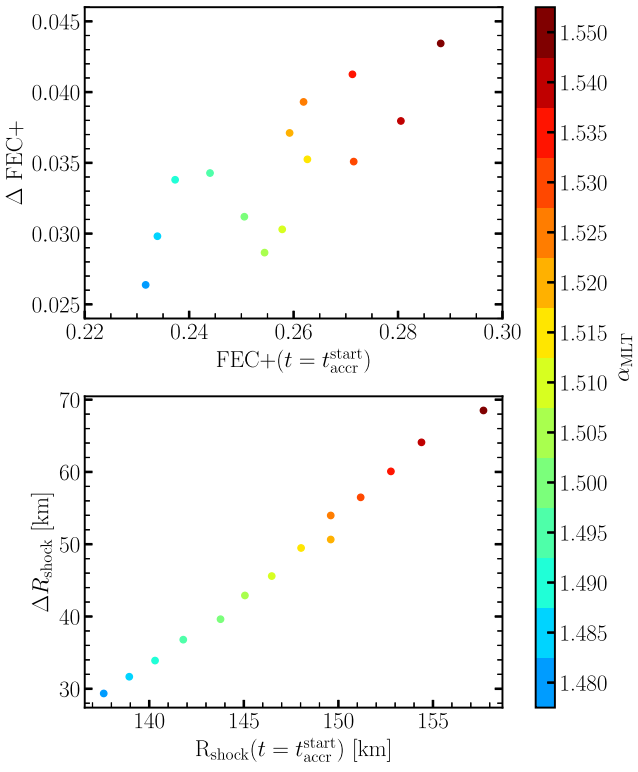


**Figure 8.** The top panel shows on the $y$-axis the increase in FEC+ due to the accretion of the Si/O interface. This quantity, i.e. $\Delta$FEC+, is simply the difference between the value of the FEC+ at $t = t^{end}_{accr}$ and at $t^{start}_{accr}$. The $x$-axis is the FEC+ at $t = t^{start}_{accr}$, the same as for Fig. 7. The times before and after accretion are shown as circles and diamonds in Fig. 6. For a description of how exactly the times before and after accretion are defined, see the text. Only simulations with $\alpha_{MLT} \geq 1.48$ are shown, since in other cases the FEC+ and shock radius do not show any significant 'jumps'. The increase in FEC+ is proportional to $\alpha_{MLT}$ and to the value of the FEC+ at $t^{start}_{accr}$, and for exploding progenitors with $\alpha_{MLT}$ around 1.51 it is between 0.03 and 0.04, which is roughly 10 per cent of the FEC+ threshold. The bottom panel is the same as the top one but for shock radius instead of FEC+ .

FEC+ at $t = t^{start}_{accr}$ (i.e. the circles in Fig. 6) and the $y$-axis is the value of the FEC+ at $t = t^{end}_{accr}$ (i.e. the diamonds in Fig. 6). Simulations with a value of FEC+ at $t = t^{start}_{accr}$ below $\sim 0.24$ do not explode, because once they accrete the interface the change in FEC+ is not enough to push it above the threshold.

As can be seen in the bottom panel of Fig. 6, the FEC+ peaks right after the accretion of the Si/O interface, before settling down to a more stable value. The reason behind this is that, as seen in the top panel, the accretion of the Si/O interface causes a sudden, extremely rapid expansion of the shock. In this transient phase, steady state is briefly disrupted and since the FEC+ is derived assuming a stalled shock solution, it cannot properly describe such rapid shock expansion, hence explaining the sudden peak in the FEC+ .

To avoid the unexplained peak of the FEC+, we define the $t^{end}_{accr}$ to be the time for which the transient phase has passed,[1] corresponding to the diamonds in Fig. 6.

All of the exploding simulations in Fig. 6 are characterized by a value of the FEC+ at $t = t^{end}_{accr}$ above 0.28–0.3.

[1]Specifically, we define $t^{end}_{accr}$ as the time $t > t^{start}_{accr}$ at which $\frac{d^2 FEC+}{dt^2}$ has the second negative peak, which means a negative change in slope of the FEC+, indicating the end of the transient period, when the FEC+ reaches a (relatively) stable steady state. Note that the first negative peak in $\frac{d^2 FEC+}{dt^2}$ occurs in correspondence with the peak in the transient phase of the FEC+.

The bottom panel of Fig. 7 shows that the values of the FEC+ at $t = t^{start}_{accr}$ and $t^{end}_{accr}$ are related to the shock radii before and after the accretion, as one would expect. Moreover, both panels show a linear correlation between FEC+ and shock radius before and after accretion, and both quantities also positively correlate with $\alpha_{MLT}$. The correlations for the FEC+ show a bit more scatter, although given the noise present in the FEC+ as a function of time (which has already been smoothed in Fig. 6) it is not surprising.

A similar correlation can be seen between $\Delta$FEC+ (or $\Delta R_{shock}$) and the value of FEC+ (or shock radius) at $t^{start}_{accr}$ (and also $\alpha_{MLT}$), as shown in Fig. 8. The quantities $\Delta$FEC+ and $\Delta R_{shock}$ are defined as the differences between the values of FEC+ and shock radius after and before the accretion of the Si/O interface. Larger $\alpha_{MLT}$, i.e. stronger $\nu$-driven convection, leads to the shock stalling at a larger radius, causing the FEC+ to be larger, and eventually, the accretion of the Si/O interface causes a proportionally larger increase in FEC+ and shock radius.

Quantitatively, we observe that during the accretion, the Si/O interface increases the FEC+ by about 0.03–0.04 (top panel of Fig. 8) for $\alpha_{MLT}$ around the best-value of 1.51. This increase is about 10 per cent of the FEC+ threshold, and it is about one-third of the

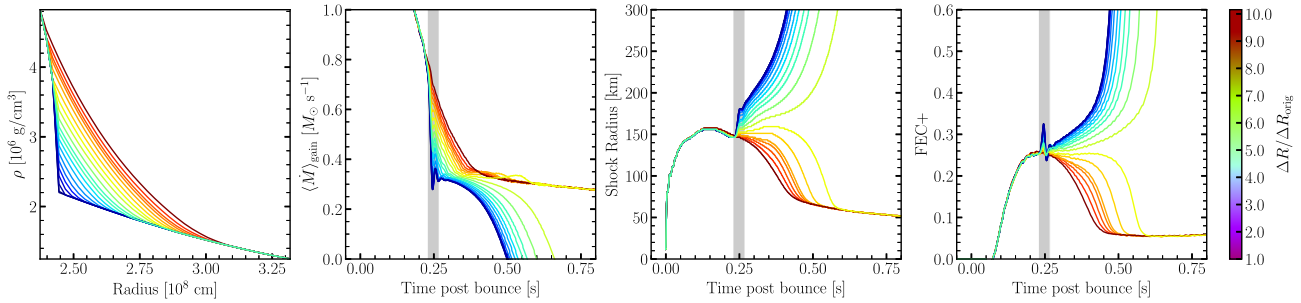


**Figure 9.** This figure refers to simulations of a 20 $M_\odot$MESA progenitor (Farmer et al. 2016) whose density at the Si/O interface has been smoothed according to the procedure outlined in the text. Larger values of $\Delta R/\Delta R_{\rm orig}$ correspond to a higher degree of smoothing. The first panel shows the pre-collapse density profile in the vicinity of the Si/O interface. The second panel shows the average mass accretion rate in the gain region as a function of time after bounce. The third panel shows the evolution of the shock radius, and the last panel shows the FEC+. The shaded region is drawn between $t_{\rm accr}^{\rm start}$ and $t_{\rm accr}^{\rm end}$, i.e. the time when the inner side of the Si/O interface is accreted and the time after the accretion and transient phase of the FEC+ has ended, as defined in Section 4.1.

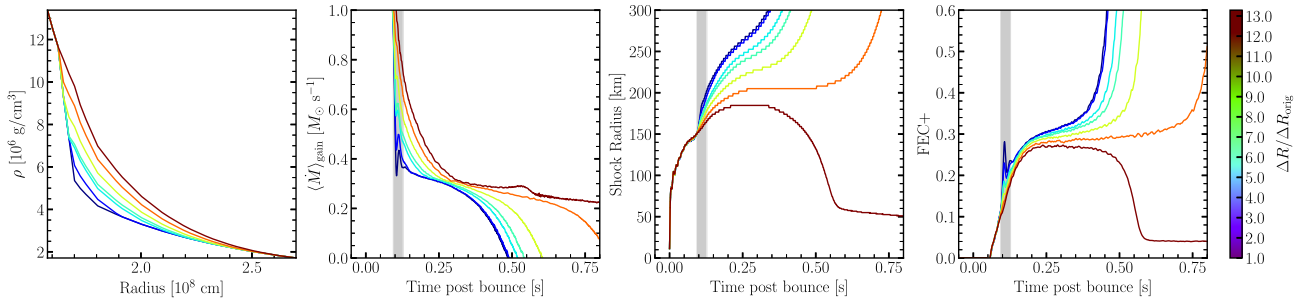


**Figure 10.** Same as Fig. 9, but for a 21 $M_\odot$ KEPLER progenitor (Sukhbold et al. 2016).

overall effect of convection, which aids the explosion condition by about 25–30 per cent (Gogilashvili et al. 2023a).

To summarize, for a given density profile with a given Si/O interface, increasing $\alpha_{\rm MLT}$ will cause the shock to stall at larger radii, increasing the overall FEC+. When the Si/O interface is accreted, the shock expansion and the increase in FEC+ will also be larger. In particular, this increase is directly proportional to both $\alpha_{\rm MLT}$ and the radius of the shock (or value of FEC+) at $t_{\rm accr}^{\rm start}$.

For a successful explosion to ensue, the FEC+ must be already close enough to the threshold (i.e. no more than 10 per cent below) when the Si/O interface is accreted.

Another conclusion that can be drawn from the present analysis is that accurately simulating the effects of the convection is crucial since it contributes to determining the time-evolution of the shock. This can significantly change the outcomes of the explosion because, as we have shown, the shock position before the accretion of the Si/O interface is strictly related to the effect of the Si/O interface accretion on the explosion condition.

In some 2D simulations, it has been shown that neutrino-driven convection is not properly captured, due to the inverse turbulent cascade caused by the imposed axisymmetry (Couch & Ott 2015). However, other studies have instead shown through detailed analysis of neutrino-driven convection that the turbulent dissipation in 2D simulations is compatible with the one found in 3D (Murphy et al. 2013; Mabanta et al. 2019), and therefore the outcomes of the simulations should be the same. Moreover, 3D simulations can suffer from finite-resolution effects, and low resolution might artificially favour the explosion (Abdikamalov et al. 2015; Radice et al. 2016). Given the uncertainties and discrepancies among different works, more systematic studies and careful investigation of neutrino-driven convection effects are necessary to improve future multidimensional simulations.

### 4.2 Sensitivity to the density drop at the Si/O interface

Another way to observe the interplay between (parametrized) neutrino-driven convection and the accretion of the Si/O interface is to study how the explosion and the FEC+ change when only the Si/O interface changes, with everything else being the same. Therefore, we artificially smoothed the density drop at the Si/O interface of two different progenitors. The first two panels of Figs 9 and 10 show the smoothing of a 20 $M_\odot$MESA progenitor (Farmer et al. 2016) and a 21 $M_\odot$ KEPLER progenitor (Sukhbold et al. 2016), respectively.

The 'degree of smoothing' shown in the colour bar of those figures is represented by the quantity $\Delta R/\Delta R_{\rm orig}$, where $\Delta R$ is the radial extent of the Si/O interface, and $\Delta R_{\rm orig}$ refers to the original progenitor without any smoothing. Therefore, a more pronounced smoothing corresponds to a larger $\Delta R$ where the density profile falls off less steeply.

After smoothing the density profile, we calculated the new pressure by imposing hydrostatic equilibrium, whereas we did not change the electron fraction $Y_{\rm e}$, which only changes by $\lesssim 1$ per cent anyway. Finally, with the new density, pressure, and electron fraction, we calculated the rest of the thermodynamic quantities by inverting the equation of state. We did not change the collapse velocities. Note that, with this procedure, we are effectively adding mass outside the Si/O interface, since the density of the smoothed profiles is larger. However, this corresponds to a maximum of 0.02 and 0.025 $M_\odot$ for the 20 $M_\odot$MESA progenitor and the 21 $M_\odot$ KEPLER progenitor, respectively. The artificially added mass is therefore small enough that it will not perturb the evolution in any way other than the change in the density jump at the Si/O interface.

One caveat that should be mentioned is that in principle this is not self-consistent since the Si/O interface corresponds to a change in composition. Therefore, one should actively change the composition

at the Si/O interface to obtain a fully consistent thermodynamic profile, which would require a self-consistent simulation. However, this is quite challenging and would potentially modify the entire thermodynamic profile, and not only the Si/O interface. Therefore, we adopted this simpler approach of directly modifying the density profile, which is the most important quantity responsible for changing the ram pressure and, consequently, the effect of the accretion of the Si/O interface through the shock.

The results of the simulations for the 20 $M_{\odot}$MESA progenitor from Farmer et al. (2016) and for the 21 $M_{\odot}$ KEPLER progenitor from Sukhbold et al. (2016) are shown in Figs 9 and 10, respectively. These two progenitors were chosen because of their large interfaces and the number of computational zones within the interface, allowing for a more accurate smoothing procedure. Moreover, the accretion of the Si/O interface occurs at $\sim 0.22$ s after bounce for the 20 $M_{\odot}$MESA progenitor, and at 0.1 s post-bounce for the 21 $M_{\odot}$ KEPLER progenitor. This allows us to study how the time of accretion changes the impact of the interface on the explosion.

The second panel of Figs 9 and 10 shows the average mass accretion rate in the gain region and, as expected, a smoother density profile at the Si/O interface corresponds to a shallower drop in mass accretion rate, which therefore prevents the shock from expanding. The third panels of those figures show the shock evolution for progenitors with different degrees of smoothing. The original progenitors explode and as the smoothing increases the shock expansion caused by the accretion of the Si/O interface becomes smaller, until eventually, it is not large enough to trigger an explosion. This can be seen by looking at the last panel, which shows that for the unmodified progenitor, the FEC+ goes above the threshold as a consequence of the accretion of the Si/O interface, resulting in an explosion. As the smoothing increases, the increase is smaller and smaller until the FEC+ is not pushed above the threshold, and therefore the star does not explode.

The 20 $M_{\odot}$MESA progenitor and the 21 $M_{\odot}$ KEPLER progenitor show the same general behaviour concerning smoothing, and the threshold of the FEC+ is at around 0.28–0.3, consistent with the one found in the simulations discussed in Sections 3 and 4.1. Moreover, the 21 $M_{\odot}$ KEPLER progenitor shows an early accretion of the Si/O interface, much like the 19.5 $M_{\odot}$ progenitor shown in Fig. 3, the difference being that the Si/O interface for the 21 $M_{\odot}$ progenitor has a larger $\delta\rho/\rho$, and therefore explodes early. However, as the degree of smoothing increases, one can see that for $\Delta R/\Delta R_{\rm orig} \approx 10$ (i.e. the orange curve in Fig. 10) the 21 $M_{\odot}$ progenitor has very similar behaviour to the 19.5 $M_{\odot}$ progenitor. An early accretion of a relatively large Si/O interface leads to the shock stalling at a large radius, and the FEC+ being pushed just below threshold. Eventually, the FEC+ slowly increases and the star explodes a few hundred milliseconds later. If one increases the smoothing further, the star does not explode.

This confirms that the explosion scenario (ii) in Section 3, i.e. where the explosion is indirectly triggered by an early accretion of a large Si/O interface followed by a late explosion, is indeed an 'edge case'. The accretion of the Si/O interface needs to be quite early, and the density drop should not be too small, like in the case of the 15.5 $M_{\odot}$ progenitor in Fig. 3. It should also not be too large, like in the case of the 21 $M_{\odot}$ progenitor studied here, which eventually behaves like the 19.5 $M_{\odot}$ progenitor in Fig. 3 only when the density drop is artificially smoothed.

This study shows how important it is to properly calculate the Si/O interface. This is no easy feat, given the complexity of stellar evolution calculations. For one these shells may or may not be a consequence of how 1D stellar evolution models handle the boundaries between stable layers and convectively unstable layers, which are inherently 3D, and even in simple 1D calculations, shell mergers might occur depending on how the convective boundaries evolve. In addition, it is well known that reduced burning networks, which decrease the computational cost and facilitate convergence, can be quite unreliable at the late stages of post-main-sequence evolution of massive stars (Farmer et al. 2016; Renzo et al. 2024).

## 5 CORRELATIONS BETWEEN SI/O INTERFACE AND FEC+

In Section 4.1, we showed how the change of the FEC+ induced by the accretion of the Si/O interface is proportional to the strength of neutrino-driven convection, and also to the value of the FEC+ itself right before the accretion. In this section, we quantify how the Si/O interface impacts the explosion by calculating the changes in the FEC+ caused by the accretion of the Si/O interface across the 341 progenitors analysed in Section 3.

First, one has to distinguish among the three major outcomes, displayed in Fig. 11 with three different colour schemes: (1) failed explosions shown as black dots; (2) high-compactness progenitors that usually explode before the accretion of the Si/O interface, shown as purple dots; (3) explosions caused by the accretion of the Si/O interface, shown as coloured dots and crosses.

First, we focus our analysis on how the value of the FEC+ at $t = t_{\rm accr}^{\rm start}$ is related to the value of the FEC+ at $t = t_{\rm accr}^{\rm end}$ (left panel of Fig. 11). We define the time before (after) accretion as the time when the inner (outer) side of the Si/O interface, i.e. the left (right) edge of the rectangles in the right panel of Fig. 3 is accreted through the shock. This definition accurately captures the change in FEC+ for failed explosions (black dots) and high-compactness progenitors (purple dots). However, one needs to be more careful when the explosion occurs after the accretion of the Si/O interface (rainbow-coloured dots). These cases are handled by defining the 'time after accretion' as the time after which the transient phase has ended, as explained in Section 4.1.

For the failed explosions (black dots) one expects scatter around the bisector. The reason is that when the Si/O interface is small (and therefore the explosion fails) it will not modify much the FEC+, and therefore the FEC+ before and after the Si/O interface is accreted through the shock should not be very different. The only exception is when the accretion happens during a rapid shock expansion (contraction), typically at early (late) times after bounce. By the time the outer edge of the Si/O interface is accreted, the FEC+ has therefore changed significantly. This explains the points above and below the bisector, for which the accretion occurs at early and late times, respectively.

For the high-compactness progenitors, shown as purple dots, one expects the FEC+ at $t = t_{\rm accr}^{\rm start}$ to be already above the threshold since, in most cases, the explosion sets in before the accretion of the Si/O interface. This is indeed confirmed by the fact that most of the purple dots are located at values of FEC+ at $t = t_{\rm accr}^{\rm start}$ larger than 0.3, indicating that the explosion has already set in. Note that there are three isolated cases in which accretion of the Si/O interface happens very early in the evolution while the shock is still expanding and has not yet reached the stalled shock phase. In these cases, while the early accretion of the Si/O interface changes the FEC+ , the main change is due to the expansion of the shock.

Finally, the exploding progenitors with $\xi_{2.0} < 0.5$ are the remaining dots and crosses, colour-coded based on the time when the accretion of the Si/O interface occurs. For these, the Si/O interface triggers an explosion, and the FEC+ quantifies why. Before the

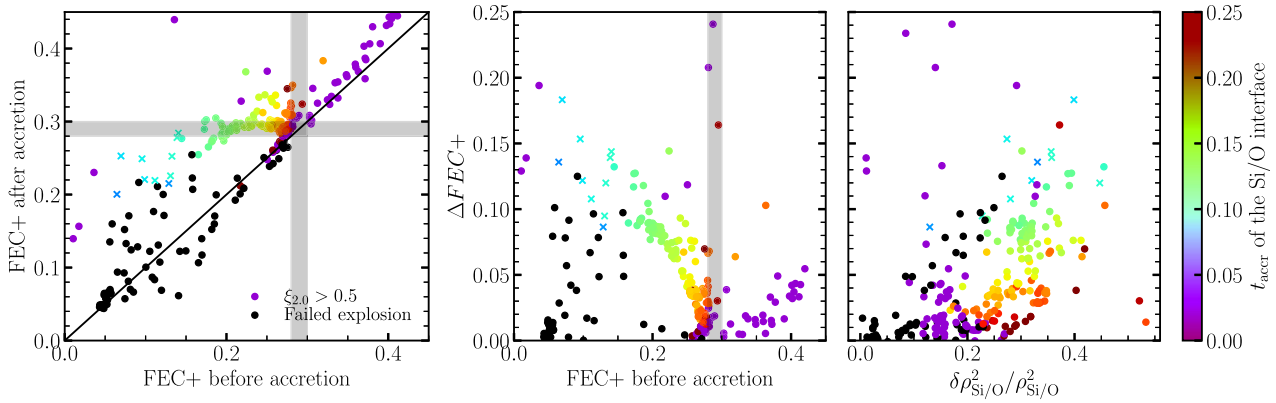


**Figure 11.** The left panel shows the values of the FEC+ at $t = t^{start}_{accr}$ and at $t^{end}_{accr}$. The FEC+ threshold is shown as a shaded region between 0.28 and 0.3 on both the $x$- and $y$-axis. The middle and right panels share the $y$-axis, which shows $\Delta$FEC+, defined as the difference between the FEC+ at $t = t^{end}_{accr}$ and at $t^{start}_{accr}$. Finally, the right panel has $\delta\rho^2_{Si/O}/\rho^2_{Si/O}$ on the $x$-axis, where $\delta_\rho$ represents the density jump at the Si/O interface in the pre-SN progenitors, and $\rho_{Si/O}$ is the density at the inner edge of the interface. The colour of the dots highlights three scenarios: (1) the simulation fails to explode even after accreting the Si/O interface (black dots); (2) the simulation explodes even before the Si/O interface accretes (purple dots); (3) the Si/O interface triggers an explosion (dots and crosses colour-coded depending on $t_{accr}$). Crosses indicate progenitors with $t_{accr} < 0.1$ s.

accretion of the Si/O interface, FEC+ is below the threshold, and after the accretion of the Si/O interface FEC+ is at or above the threshold. The progenitors shown as crosses are characterized by a very early accretion of the Si/O interface (see for example the 19.5 $M_\odot$ progenitor shown in Fig. 3) and are therefore exceptions that will be discussed later in the section.

Similar conclusions can be drawn from the middle panel, in which $\Delta$FEC+ (i.e. the difference between the FEC+ at $t = t^{end}_{accr}$ and at $t = t^{start}_{accr}$) is plotted against the value of the FEC+ at $t = t^{start}_{accr}$. The correlation between these two quantities is quite evident. The reason is that, if the accretion occurs early in the post-bounce phase, the shock is still expanding, and therefore the FEC+ is also increasing. Therefore, one expects larger $\Delta$FEC+ since not only does the accretion increase the FEC+, but the secular shock expansion also contributes to the increase. This is confirmed by the fact that simulations with early accretions (i.e. $t_{accr} \lesssim 0.2$ s) also exhibit larger $\Delta$FEC+. As mentioned above, the reason is that if the accretion of the Si/O interface occurs early enough in the post-bounce phase, then the FEC+ increases not only because of the accretion but also because of the secular shock expansion. Note that this discussion is not valid for failed explosions and high-compactness progenitors.

In the last panel, we show $\Delta$FEC+ as a function of $\delta\rho^2_{Si/O}/\rho^2_{Si/O}$, where $\rho^2_{Si/O}$ is the density on the inner side of the Si/O interface, and $\delta\rho_{Si/O}$ is the density drop from the inner to the outer side of the interface. Examples of this are given in the rightmost panel of Fig. 3. One would naively expect larger density drops to cause larger $\Delta$FEC+, and indeed that trend is generally visible. However, it is also polluted by a large vertical scatter, which is due to early time accretions, for which not only the accretion of the Si/O interface, but also secular shock expansion contribute to $\Delta$FEC+. This is confirmed by the fact that, given the same $\delta\rho^2_{Si/O}/\rho^2_{Si/O}$, simulations where the Si/O interface is accreted at early times lead to larger $\Delta$FEC+. Therefore, if one takes into account the contribution to the FEC+ by secular shock expansion, one can find a much tighter dependence of $\Delta$FEC+ on $\delta\rho^2_{Si/O}/\rho^2_{Si/O}$. By only selecting progenitors that have a relatively similar accretion time of the Si/O interface (i.e. similar colours in the rightmost panel of Fig. 11, one can indeed see that the vertical spread becomes much narrower.

Finally, there are a few exceptions worth discussing. The crosses in Fig. 11 are progenitors characterized by early accretion of the Si/O interface, i.e. $t_{accr} < 0.1$ s. Their shock radius and FEC+ evolution are very similar to the 19.5 $M_\odot$ progenitor shown in Fig. 3. In other words, they are part of scenario (3) defined in Section 3, for which the early accretion of the Si/O interface does not push the FEC+ above the threshold, but instead pushes it very close to it, facilitating the occurrence of an explosion a few hundred milliseconds later. Therefore, one expects the FEC+ at $t = t^{end}_{accr}$ to be below the threshold, and the $\Delta$FEC+ to be very large since the earlier the accretion, the faster the shock expansion, and therefore the larger the FEC+ increase. This is indeed confirmed by the left and middle panels in Fig. 11. Most of the simulations shown as rainbow-coloured dots instead belong to scenario (2) defined in Section 3. These are cases where the accretion of a large Si/O interface occurs during the stalled shock phase, pushes the FEC+ above the threshold, and therefore causes the explosion. As seen in the left panel of Fig. 11, for some of them the FEC+ at $t = t^{end}_{accr}$ is, however, below the threshold, and $t_{accr} > 0.1$ s. These can be thought of as intermediate cases between scenarios (2) and (3). The accretion of the Si/O interface occurs at the very beginning of the stalled shock phase.

### 5.1 Quantitative effect of Si/O interface accretion on the explosion condition

In Section 4.1 we already compared the magnitude of $\Delta$FEC+ with the overall explosion threshold of 0.28–0.3. However, that was done only for one progenitor, and we found that $\Delta$FEC+ is about 10 per cent of the explosion condition. With the much larger sample of 341 progenitors, we can perform the same exercise and estimate the average impact that the Si/O interface has on the explosion condition. This is not a straightforward task since, as explained above, the secular shock expansion can sometimes overlap with the increase in FEC+ due to the Si/O interface accretion. Therefore, we exclude all of the high-compactness progenitors from the subsequent analysis, since as explained above the vast majority accreted the Si/O interface after the explosion has started. Then, we limit our sample to exploding progenitors that accrete the Si/O interface during the stalled-shock phase, when changes

**Table 1.** Statistical measures of ΔFEC+ for different samples, which include all exploding progenitors with $\xi_{2.0} < 0.5$, and further restricted based on the condition described in the first column. The second column shows the size of the sample (i.e. how many simulations satisfy that condition), and the remaining columns are the mean, median, and 10, 25, 75, and 90 per cent quantiles. The percentage in parenthesis is calculated by dividing the number by the FEC+ threshold (i.e. 0.29), and it therefore shows how much the accretion of the Si/O interface contributes to the overall explosion condition. The first row includes all exploding progenitors with $\xi_{2.0} < 0.5$. The next four rows restrict the population further based on the accretion time of the Si/O interface. The last four rows restrict the population further based on the value of the FEC+ right before the accretion of the Si/O interface. The second to last row represents the most reliable population (see the text).

| Condition | $N_{\rm sample}$ | Mean | Median | $Q_{10\ \rm per\ cent}$ | $Q_{25\ \rm per\ cent}$ | $Q_{75\ \rm per\ cent}$ | $Q_{90\ \rm per\ cent}$ |
|---|---|---|---|---|---|---|---|
| All | 129 | 0.059 (20 per cent) | 0.053 (18 per cent) | 0.018 (6 per cent) | 0.034 (12 per cent) | 0.084 (29 per cent) | 0.096 (33 per cent) |
| $t_{\rm accr} > 0.12$ | 123 | 0.056 (19 per cent) | 0.048 (17 per cent) | 0.018 (6 per cent) | 0.033 (11 per cent) | 0.082 (28 per cent) | 0.090 (31 per cent) |
| $t_{\rm accr} > 0.15$ | 116 | 0.052 (18 per cent) | 0.044 (15 per cent) | 0.018 (6 per cent) | 0.032 (11 per cent) | 0.077 (27 per cent) | 0.088 (30 per cent) |
| $t_{\rm accr} > 0.18$ | 75 | 0.035 (12 per cent) | 0.035 (12 per cent) | 0.015 (5 per cent) | 0.022 (8 per cent) | 0.042 (15 per cent) | 0.061 (21 per cent) |
| $t_{\rm accr} > 0.2$ | 46 | 0.027 (9 per cent) | 0.027 (9 per cent) | 0.011 (4 per cent) | 0.018 (6 per cent) | 0.036 (12 per cent) | 0.039 (13 per cent) |
| FEC+ > 0.2 | 104 | 0.047 (16 per cent) | 0.039 (13 per cent) | 0.017 (6 per cent) | 0.029 (10 per cent) | 0.070 (24 per cent) | 0.084 (29 per cent) |
| FEC+ > 0.22 | 87 | 0.040 (14 per cent) | 0.037 (13 per cent) | 0.015 (5 per cent) | 0.024 (8 per cent) | 0.053 (18 per cent) | 0.070 (24 per cent) |
| FEC+ > 0.24 | 75 | 0.036 (12 per cent) | 0.035 (12 per cent) | 0.015 (5 per cent) | 0.022 (8 per cent) | 0.042 (15 per cent) | 0.064 (22 per cent) |
| FEC+ > 0.26 | 49 | 0.029 (10 per cent) | 0.029 (10 per cent) | 0.013 (4 per cent) | 0.018 (6 per cent) | 0.037 (13 per cent) | 0.041 (14 per cent) |

to the FEC+ can be attributed exclusively to the accretion of the interface, rather than to secular shock expansion. This can be achieved by excluding all progenitors for which the accretion of the interface occurs before a certain time or, alternatively, by excluding all progenitors for which the FEC+ at $t = t_{\rm accr}^{\rm start}$ is below a certain value. Depending on the chosen condition, the sample will be different.

In Table 1, we show how different cuts on $t_{\rm accr}$ and the value of the FEC+ at $t = t_{\rm accr}^{\rm start}$ affect the sample size. Then, for the progenitors that satisfy those conditions, we calculate the median, mean, and selected quantiles of ΔFEC+. We find the conditions $t_{\rm accr} > 0.18$ s and FEC+ > 0.24 to lead to almost the same sample. We also consider them to be the best cuts since they include as many simulations as possible, without, however, including cases where significant secular shock expansion is occurring alongside the accretion of the Si/O interface. Note that the condition that the FEC+ at $t = t_{\rm accr}^{\rm start}$ should be > 0.24 is the same found in Section 4.1 in order for the 20 $M_\odot$ MESA progenitor to explode. For both samples, the median ΔFEC+ is $\sim 0.035$, which is in line with what was found for the 20 $M_{\odot\rm MESA}$ progenitor, and it is $\sim 10$ per cent of the explosion condition, to be compared with the 25–30 per cent effect of convection (Gogilashvili et al. 2023a). The first and third quartiles are $\sim 0.023$ and $\sim 0.046$, which correspond to $\sim 8$ and $\sim 15$ per cent of the explosion condition, and more than 90 per cent of the simulations have ΔFEC+ > 0.015, corresponding to $\sim 5$ per cent of the explosion condition. This shows that the accretion of the Si/O interface has a crucial impact on the explosion of progenitors with compactness $\xi_{2.0} < 0.5$. This impact can be quantified to be between 5 and 15 per cent of the overall explosion condition, or equivalently between 20 and 50 per cent of the effect of convection.

## 6 CONCLUSIONS

In this paper, we analysed the post-bounce phase of 341 1D+ simulations using the generalized Force Explosion Condition (FEC+). We found that when the FEC+ goes beyond the threshold, empirically found to be around 0.28–0.3, an explosion ensues. We identified three scenarios where an explosion is achieved: (1) High-compactness progenitors tend to always explode, often before accreting the Si/O interface; (2) lower compactness progenitors, with $\xi_{2.0} \lesssim 0.5$, achieve an explosion if a large enough density drop ($\delta\rho^2_{\rm Si/O}/\rho^2_{\rm Si/O} > 0.08$) is accreted through the shock during the stalled-shock phase; (3) a progenitor with $\xi_{2.0} \lesssim 0.5$ achieves an explosion significantly after the accretion of a large density drop before the stalled-shock phase.

For failed explosions, we identified three scenarios: (4) a progenitor with $\xi_{2.0} \lesssim 0.5$ accretes a large density drop before the stalled-shock phase, although smaller than in scenario (3), and therefore not sufficient to cause an explosion; (5) a progenitor with $\xi_{2.0} \lesssim 0.5$ accretes a small density drop ($\delta\rho^2_{\rm Si/O}/\rho^2_{\rm Si/O} < 0.08$) during the stalled-shock phase; (6) a progenitor with $\xi_{2.0} \lesssim 0.5$ accretes either a small or large density drop late in the stalled-shock phase when the shock cannot be revived anymore.

In all cases, the explosions ensue only when the FEC+ crosses the threshold of 0.28–0.3, showing that the FEC+ is a robust tool to describe the explosion condition.

We also studied how the FEC+ (and therefore the explosion) varies depending on the strength of $\nu$-driven convection (i.e. the mixing-length parameter $\alpha_{\rm MLT}$). We again showed that the explosion occurs only when the FEC+ goes above the threshold of 0.28–0.3 empirically derived in Section 3, which confirms the robustness of the FEC+ as an explosion condition. We showed that the value of the FEC+ at $t = t_{\rm accr}^{\rm start}$, as well as the change in FEC+ caused by the accretion of the Si/O interface, are positively correlated. They also positively correlate with $\alpha_{\rm MLT}$, the radius of the stalled shock, and the increase in shock radius caused by the accretion of the interface. This confirms the key role that convection has in aiding the explosion, which is extremely important since it has been shown that, for example, three-dimensional asymmetries in the pre-SN progenitor (Couch et al. 2015; Müller et al. 2016b; Yoshida et al. 2019; Yadav et al. 2020; Fields & Couch 2021) can significantly change the strength of convection that develops in the post-bounce phase. Moreover, it is still unclear if and how numerical resolution (Abdikamalov et al. 2015; Radice et al. 2016) or the dimensionality of the problem (Murphy et al. 2013; Couch & Ott 2015) can artificially alter the efficiency of convection.

Moreover, we show that the change in the FEC+ due to the accretion of the Si/O interface becomes progressively smaller by artificially smoothing the density drop at the Si/O interface. Eventually, for a large enough smoothing parameter, the FEC+ drops below the threshold causing the originally successful explosion to fail. Once again, we verified that the threshold in these simulations is also at around 0.28–0.3. We conclude that for progenitors with low to intermediate compactness ($\xi_{2.0} \lesssim 0.5$), the presence of a large

density drop at the Si/O interface is crucial to determine whether or not an explosion occurs.

Finally, we analysed how the change in FEC+ is related to the value of the FEC+ right before the accretion of the Si/O interface through the shock, and also to the density drop at the Si/O interface $\delta\rho^2_{\rm Si/O}/\rho^2_{\rm Si/O}$. We concluded that for the accretion of the Si/O interface to lead to successful explosions, the FEC+ should already be close to the explosion threshold, depending on how large the density drop at the Si/O interface is. We then quantified the effect of the Si/O interface accretion by analysing the exploding progenitors with $\xi_{2.0} \lesssim 0.5$.

The analysis for progenitors accreting the interface early (i.e. before $\sim 0.18$ s after bounce) is complicated by the fact that the FEC+ changes not only because of the shock expansion caused by the accretion of the Si/O interface but also because of a secular shock expansion. By focusing only on progenitors where the secular shock expansion is negligible, we find that the accretion of the Si/O interface can contribute between 5 and 15 per cent to the overall explosion condition, i.e. between 20 and 50 per cent of the overall effect of convection, which has been estimated to decrease the explosion condition by about 25–30 per cent (Gogilashvili et al. 2023a).

The FEC+ is a powerful tool to analyse the post-bounce phase of the CCSN, and can be also applied to multidimensional simulations, where, however, more complex phenomena and geometries are at play, and therefore more careful analysis is required. These 1D+ simulations showed that the interplay between neutrino-driven convection and the accretion of the Si/O interface can be crucial for the explosion, and therefore future CCSN simulations should ensure that convection is properly resolved and carefully analysed.

Moreover, it is important to utilize (and also simulate!) pre-collapse models whose late stages of evolution have been carefully calculated. Since the density drop at the Si/O interface plays such a crucial role in the explosion, contributing to roughly 10 per cent of the overall explosion condition, detailed stellar evolution models are required in order to accurately simulate the last few months of the life of massive stars, where shell Si-burning becomes important and can drastically modify the density discontinuity at the interface with the oxygen shell.

## ACKNOWLEDGEMENTS

The authors acknowledge the hosts and organizers of MICRA 2023 at ECT∗ for facilitating discussions on this project. LB is supported by the U.S. Department of Energy under grant no. DE-SC0004658. LB would like to thank the N3AS centre for their hospitality and support. EPO is supported by the Swedish Research Council (Project No. 2020–00452). MG and JM acknowledge support from the Laboratory Directed Research and Development program, the Center for Space and Earth Sciences, and the Center for Nonlinear Studies under project numbers 20240477CR-SES and 20220564ECR at Los Alamos National Laboratory (LANL). LANL is operated by Triad National Security, LLC, for the National Nuclear Security Administration of U.S. Department of Energy (contract no. 89233218CNA000001). MG acknowledges support from the Danmarks Frie Forskningsfond (Project No. 8049-00038B, PI: I. Tamborra). This article is cleared for unlimited release, LA-UR-24-30985.

## DATA AVAILABILITY

The data are available upon reasonable request to the corresponding author.

## REFERENCES

Abdikamalov E. et al., 2015, ApJ, 808, 70
Andresen H., Müller B., Müller E., Janka H. T., 2017, MNRAS, 468, 2032
Bethe H. A., Wilson J. R., 1985, ApJ, 295, 14
Boccioli L., Fragione G., 2024, Phys. Rev. D, 110, 023007
Boccioli L., Mathews G. J., O'Connor E. P., 2021, ApJ, 912, 29
Boccioli L., Mathews G. J., Suh I.-S., O'Connor E. P., 2022, ApJ, 926, 147
Boccioli L., Roberti L., Limongi M., Mathews G. J., Chieffi A., 2023, ApJ, 949, 17
Bollig R., Yadav N., Kresse D., Janka H.-T., Müller B., Heger A., 2021, ApJ, 915, 28
Bruenn S. W., 1985, ApJS, 58, 771
Bruenn S. W., Mezzacappa A., Hix W. R., Blondin J. M., Marronetti P., Messer O. E. B., Dirk C. J., Yoshida S., 2009, J. Phys. Conf. Ser., 180, 012018
Buras R., Rampp M., Janka H. T., Kifonidis K., 2006, A&A, 447, 1049
Burrows A., Goshy J., 1993, ApJ, 416, L75
Burrows A., Vartanyan D., 2021, Nature, 589, 29
Burrows A., Vartanyan D., Dolence J. C., Skinner M. A., Radice D., 2018, Space Sci. Rev., 214, 33
Burrows A., Radice D., Vartanyan D., Nagakura H., Skinner M. A., Dolence J. C., 2020, MNRAS, 491, 2715
Burrows A., Wang T., Vartanyan D., 2024, preprint (arXiv:2412.07831)
Cabezón R. M., Pan K.-C., Liebendörfer M., Kuroda T., Ebinger K., Heinimann O., Perego A., Thielemann F.-K., 2018, A&A, 619, A118
Colgate S. A., White R. H., 1966, ApJ, 143, 626
Couch S. M., Ott C. D., 2015, ApJ, 799, 5
Couch S. M., Chatzopoulos E., Arnett W. D., Timmes F. X., 2015, ApJ, 808, L21
Couch S. M., Warren M. L., O'Connor E. P., 2020, ApJ, 890, 127
Diehl R. et al., 2021, Publ. Astron. Soc. Aust., 38, e062
Eggenberger Andersen O., Zha S., da Silva Schneider A., Betranhandy A., Couch S. M., O'Connor E. P., 2021, ApJ, 923, 201
Eggenberger Andersen O., O'Connor E., Andresen H., da Silva Schneider A., Couch S. M., 2024, preprint (arXiv:2411.11969)
Ertl T., Janka H. T., Woosley S. E., Sukhbold T., Ugliano M., 2016, ApJ, 818, 124
Farmer R., Fields C. E., Petermann I., Dessart L., Cantiello M., Paxton B., Timmes F. X., 2016, ApJS, 227, 22
Fernández R., 2012, ApJ, 749, 142
Fernández R., 2015, MNRAS, 452, 2071
Fields C. E., Couch S. M., 2021, ApJ, 921, 28
Foglizzo T., Scheck L., Janka H. T., 2006, ApJ, 652, 1436
Fryer C. L., Warren M. S., 2002, ApJ, 574, L65
Fryer C. L., Belczynski K., Wiktorowicz G., Dominik M., Kalogera V., Holz D. E., 2012, ApJ, 749, 91
Fryer C. L., Olejak A., Belczynski K., 2022, ApJ, 931, 94
Glas R., Just O., Janka H. T., Obergaulinger M., 2019, ApJ, 873, 45
Gogilashvili M., Murphy J. W., 2022, MNRAS, 515, 1610
Gogilashvili M., Murphy J. W., Miller J. M., 2023a, ApJ, 962, 8
Gogilashvili M., Murphy J. W., O'Connor E. P., 2023b, MNRAS, 524, 4109
Hempel M., Schaffner-Bielich J., 2010, Nucl. Phys. A, 837, 210
Herant M., Benz W., Hix W. R., Fryer C. L., Colgate S. A., 1994, ApJ, 435, 339
Horowitz C. J., 2002, Phys. Rev. D, 65, 043001
Horowitz C. J., Caballero O. L., Lin Z., O'Connor E., Schwenk A., 2017, Phys. Rev. C, 95, 025801
Janka H. T., 2001, A&A, 368, 527
Janka H.-T., 2012, Ann. Rev. Nucl. Part. Sci., 62, 407
Janka H. T., Bauswein A., 2023, in Tanihata I., Toki H., Kajino T., eds, Handbook of Nuclear Physics. Springer Nature, Singapore, p. 4005
Lattimer J. M., Swesty D. F., 1991, Nucl. Phys. A, 535, 331
Lentz E. J. et al., 2015, ApJ, 807, L31
Mabanta Q. A., Murphy J. W., 2018, ApJ, 856, 22
Mabanta Q. A., Murphy J. W., Dolence J. C., 2019, ApJ, 887, 43
Marek A., Janka H. T., 2009, ApJ, 694, 664
Müller B., 2016, Publ. Astron. Soc. Aust., 33, e048

Müller B., 2019, MNRAS, 487, 5304
Müller B., 2020, Liv. Rev. Comput. Astrophys., 6, 3
Müller B., Heger A., Liptai D., Cameron J. B., 2016a, MNRAS, 460, 742
Müller B., Viallet M., Heger A., Janka H.-T., 2016b, ApJ, 833, 124
Murphy J. W., Burrows A., 2008, ApJ, 688, 1159
Murphy J. W., Dolence J. C., 2017, ApJ, 834, 183
Murphy J. W., Meakin C., 2011, ApJ, 742, 74
Murphy J. W., Dolence J. C., Burrows A., 2013, ApJ, 771, 52
Nakamura K., Takiwaki T., Kotake K., 2022, MNRAS, 514, 3941
Nakamura K., Takiwaki T., Matsumoto J., Kotake K., 2024, MNRAS, 536, 280
Neustadt J. M. M., Kochanek C. S., Stanek K. Z., Basinger C., Jayasinghe T., Garling C. T., Adams S. M., Gerke J., 2021, MNRAS, 508, 516
O'Connor E., 2015, ApJS, 219, 24
O'Connor E. P., Couch S. M., 2018a, ApJ, 854, 63
O'Connor E. P., Couch S. M., 2018b, ApJ, 865, 81
O'Connor E., Ott C. D., 2010, Class. Quantum Gravity, 27, 114103
O'Connor E., Ott C. D., 2011, ApJ, 730, 70
Patton R. A., Sukhbold T., 2020, MNRAS, 499, 2803
Pejcha O., Thompson T. A., 2012, ApJ, 746, 106
Powell J., Müller B., Heger A., 2021, MNRAS, 503, 2108
Radice D., Ott C. D., Abdikamalov E., Couch S. M., Haas R., Schnetter E., 2016, ApJ, 820, 76
Radice D., Abdikamalov E., Ott C. D., Mösta P., Couch S. M., Roberts L. F., 2018, J. Phys. G Nucl. Phys., 45, 053003
Renzo M., Goldberg J. A., Grichener A., Gottlieb O., Cantiello M., 2024, Res. Notes Am. Astron. Soc., 8, 152
Salpeter E. E., 1955, ApJ, 121, 161
Sasaki S., Takiwaki T., 2024, MNRAS, 528, 1158
Steiner A. W., Hempel M., Fischer T., 2013, ApJ, 774, 17
Sukhbold T., Ertl T., Woosley S. E., Brown J. M., Janka H. T., 2016, ApJ, 821, 38
Summa A., Hanke F., Janka H.-T., Melson T., Marek A., Müller B., 2016, ApJ, 825, 6
Summa A., Janka H.-T., Melson T., Marek A., 2018, ApJ, 852, 28
Sykes B., Müller B., 2024, preprint (arXiv:2410.04944)
Takiwaki T., Kotake K., Suwa Y., 2016, MNRAS, 461, L112
Thompson T. A., Quataert E., Burrows A., 2005, ApJ, 620, 861
Tsang B. T. H., Vartanyan D., Burrows A., 2022, ApJ, 937, L15
Wang T., Vartanyan D., Burrows A., Coleman M. S. B., 2022, MNRAS, 517, 543
Woosley S. E., Heger A., Weaver T. A., 2002, Rev. Mod. Phys., 74, 1015
Yadav N., Müller B., Janka H. T., Melson T., Heger A., 2020, ApJ, 890, 94
Yamasaki T., Yamada S., 2005, ApJ, 623, 1000
Yoshida T., Takiwaki T., Kotake K., Takahashi K., Nakamura K., Umeda H., 2019, ApJ, 881, 16

This paper has been typeset from a TEX/LATEX file prepared by the author.